scientific reports

OPEN

Vibrational characteristics of aluminum–phosphate compounds by an experimental and theoretical approach

Pawel Goj✉, Bartosz Handke & Pawel Stoch

Aluminum phosphates are materials with relatively wide potential applications in many industries. The vibrational features of selected compounds were established on Raman and infrared spectroscopy. The experimentally determined spectra are compared to those calculated by ab initio methods. This gives a unique possibility of a proper assignment of the experimental spectral features to specific modes of vibration. In the results, it was evidenced that the spectra are characterized by two specific intense bands in the mid- and high-frequency range due to the P–O–P and P–O bonds in [PO₄] tetrahedron vibrations. The position of the high-frequency band is related to the number of bridging oxygen atoms connecting [PO₄] tetrahedrons in the unit cell. Additionally, the differences in the spectra were evidenced as a result of different polymorphic forms of the selected compounds. Therefore, the results may be useful in determining the phase composition of polyphase materials or structural features of aluminum–phosphate glasses and glass–ceramic materials.

Aluminum phosphates are present in many applications, for example in chemically bonded phosphate ceramics (CBPC) with alumina, dental cement, refractory binders, composite materials, and glass–ceramics[1–10]. Pyrophosphates containing aluminum and monovalent cations, such as $NaAlP_2O_7$, can be used as solid electrolytes for batteries, piezoelectric and ionic conductors[11–13]. Furthermore, $NaAlP_2O_7$ with different doped rare earth ions has potential application in white light emitting diodes (WLEDS)[14,15]. In the group of aluminum phosphates are molecular sieves (AlPO) that can be used in catalysis, separation, and ion exchange[16–18].

Raman and infrared spectroscopies (IR), in addition to X-ray diffraction (XRD), are one of the most important methods of structural characterization of different materials. The spectroscopies are especially important in the case of amorphous materials such as glasses, where, because of the lack of long-range order, application of XRD is strongly limited. In this method, the proper assignment of characteristic bands to specific vibrations is a crucial point. To solve the problem, calculation methods based on density functional theory (DFT) can be very helpful. The methods allow for the prediction of theoretical IR and Raman spectra with considerable precision[19–23].

The aim of the work was to compare theoretical and experimental IR and Raman spectra of different aluminum-phosphate compounds. Additionally, the theoretical results were used to determine the proper assignment of the characteristic spectral features to the different vibration modes. Special attention was paid to the position of the bands related to bond vibrations in the [PO₄] tetrahedrons. The structural elements are the main building blocks of the aluminum phosphate compounds. Moreover, it is interesting to observe their changes resulting from structural transformations e.g. from chain to ring structures that may be evidenced in the compounds.

In the work, the Q^i notation is applied as commonly used in phosphate glasses[19,24]. In this notation, 'Q' means phosphorus tetrahedron [PO₄], and 'i' is a number of other phosphorus tetrahedra connected to 'Q'. Aluminum phosphates were chosen so that all Q^i structural units were represented in the studies. Only the structural units Q^3 are in pure P_2O_5, where the most stable polymorphic form is o'-P_2O_5[25]. Pure Q^2 units are characteristic for $Al(PO_3)_3$, which has three polymorphs. A-$Al(PO_3)_3$ and aluminum cyklohexaphosphate, which have 4- and 6-membered [PO₄] rings, respectively. Although B-$Al(PO_3)_3$ has a chain structure[4,26–28]. Aluminum cyklohexaphosphate and B-$Al(PO_3)_3$ are stable at temperatures lower than 800 °C but detailed studies have not been carried out. Above 800 °C, mainly A-$Al(PO_3)_3$ has been reported (Fig. 1)[4,28–30]. There is no pure

Faculty of Materials Science and Ceramics, AGH-University of Science and Technology, Al. Mickiewicza 30, 30-059 Kraków, Poland. ✉email: pgoj@agh.edu.pl
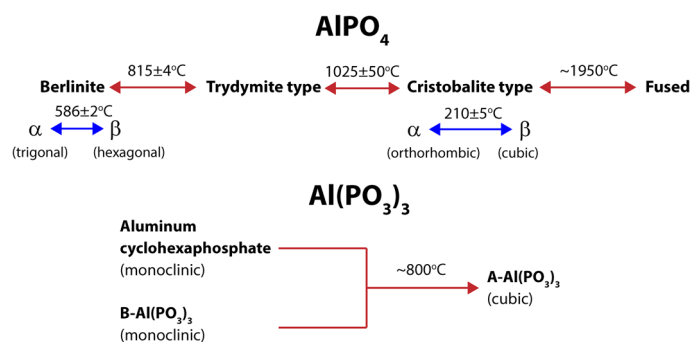
Figure 1. Thermal transformations of $AlPO_4$ and $Al(PO_3)_3$. Crystal system in parentheses. Ref[4,28,30,33,38–41].
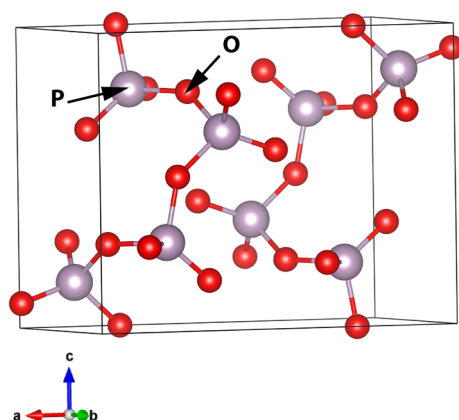

Figure 2. The unit cell of o'-P_2O_5 with optimized atom positions.

aluminum–phosphate compound in which there are only Q^1 units. Therefore, sodium-containing $NaAlP_2O_7$ was chosen. In the crystal structure, $P_2O_7^{4-}$ dimers are present that are two joined Q^1 structural units. The case of Q^0 is represented by AlPO4, which is one of the most studied compounds of aluminum phosphates[4,7,31–37]. $AlPO_4$ is a high refractory material with a melting point of about 1950 °C[38] but a glaze on the surface due to probably the loss of P_2O_5 can be detected[32]. It undergoes several phase transformations, as shown in Fig. 1[39], and the phases are isostructural to SiO_2.

In the work low-temperature form of berlinite (α-berlinite) which is isostructural to α-quartz and low-temperature α-cristobalite type $AlPO_4$ that has a close similar structure to α-cristobalite[31,33] were studied.

Although the selected compounds are known, the number of literature data concerning their vibrational features is relatively limited. To the best of our knowledge, this is the first report in which all of the compounds are gathered together, and their experimental spectra are compared with the theoretical ones.

Results

o'-P_2O_5. The DFT optimized unit cell of o'-P_2O_5 is shown in Fig. 2. In the unit cell, there exist only Q^3 structural units. In the unit cell, 3 bridging oxygens are involved in the formation of P–O_B–P bridges, and one is double-bonded to oxygen P=O. There are two inequivalent phosphorous sites with the mean P–O bond lengths 1.573 Å, 1.446 Å for P–O_B and P=O, respectively. The shorter length of the P=O bond leads to distortion of the [PO_4] tetrahedron with the off-center shift of the central atom. The calculated Raman and IR intensities and their assignments are summarized in detail in Table S1.1 (supplementary materials). The calculated vibrations for o'-P_2O_5 were assigned to the vibrations of the idealized Q^3 molecule (points group C_{3v}) and idealized P-O_B-P bridge (points group C_{2v}). (Fig. S1.1 and S1.2 supplementary material).

Figure 3 shows the calculated Raman and IR spectra, and the simplified frequency ranges of the specific vibrations are summarized in Table 1. As can be seen in the Raman spectrum the most intense bands are at 604 cm^{-1} and 1300, 1344 cm^{-1}. The lower frequency band is related to the symmetric (A_1) and symmetric deformation (E) of 3(P-O_B) in Q^3. The higher value is due to the stretching of P=O in Q^3 units. Other vibrations are considerably weaker. In the case of the IR spectrum, the strongest bands at 937 and 957 cm^{-1} are related to asymmetric stretching of P–O_B–P and 3(P–O) in Q^3. In this case, the bands due to P=O vibrations are also present, although their intensities are considerably lower.

It should be noted that in this case, we present only theoretical spectra that were not scaled or shifted.
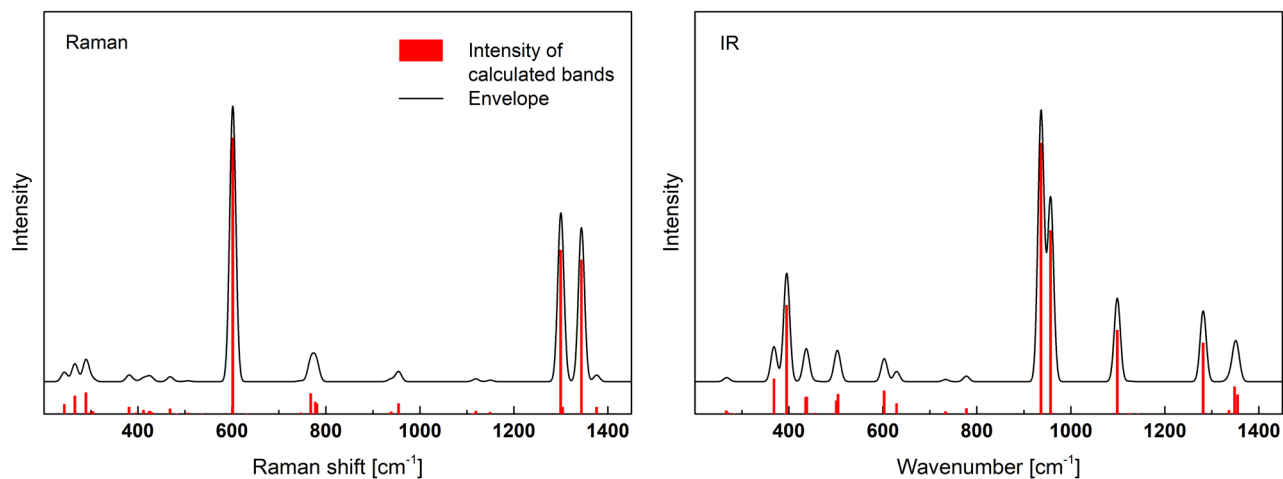
Figure 3. Calculated Raman and IR spectra of o'-P_2O_5.

Frequency (>200) [cm^{-1}]	Intensity Raman (the most intense frequencies [cm^{-1}])	Intensity IR (the most intense frequencies [cm^{-1}])	Assignment to Q^i idealized vibrations and P–O$_B$–P
<300	Weak (244, 266 and 290 (s))	Very weak	Lattice vibrations and librations
368–483	Very weak	Medium (368, 395 (s), 435 and 438)	Asymmetric deformation (E) of 3(P-O$_B$) in Q^3
505–633	Very strong (602(s))	Weak (505, 603 (s))	Symmetric (A$_1$) and asymmetric (E) deformation of 3(P-O$_B$) in Q^3 in different positions and Bending (A$_1$) in P-O$_B$-P
734–781	Weak (768, 778 and 781)	Very weak	Symmetric stretching (A$_1$) in P-O$_B$-P
936–939	Very weak	Very strong. (937 (s))	Asymmetric stretching (B$_1$) in P-O$_B$-P
955–957	Weak (955 (s))	Strong (957 (s))	Asymmetric stretching (E) of 3(P-O) in Q^3
1099–1150	Very weak	Medium (1099 (s))	Symmetric (A$_1$) and Asymmetric (E) stretching of 3(P-O$_B$) in Q^3 in different positions
1282–1376	Very strong (1300 (s) and 1344)	Medium (1282, 1349 (s) and 1355)	Symmetric stretching (A$_1$) of P = O$_{NB}$ in Q^3

Table 1. The calculated Raman and IR active modes of o'-P_2O_5 (more details in the supplementary material Table S1.1). s—the strongest in range.
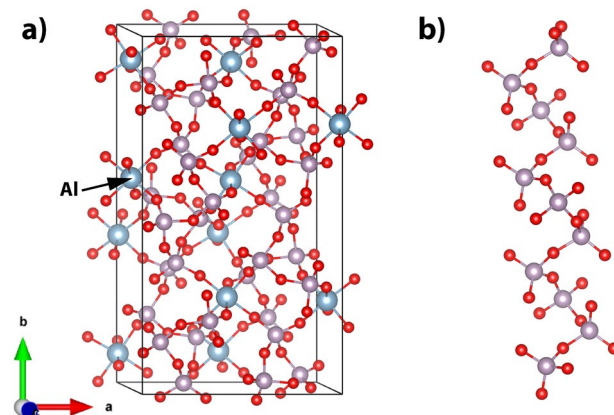

Figure 4. (**a**) Unit cell of B-Al(PO$_3$)$_3$ with the optimized atoms' positions and (**b**) chain of Q^2 structural units.

B-Al(PO$_3$)$_3$. The B-Al(PO$_3$)$_3$ is made up of infinitely twisted chains of structural units connected by [AlO$_6$] octahedra. The unit cell is shown in Fig. 4. The length of the P-O$_B$ bond changes in the range of 1.570–1.600 Å, whereas that of P-O$_{NB}$ varies in the range of 1.480–1.488 Å. It should be pointed out that in the crystal structure there are no pure double-bonded oxygen atoms (P=O). All the non-bridging oxygens form P-O$_{NB}$-Al bridges, and the excess phosphorus positive charge is redistributed over the two P-O$_{NB}$ bonds.
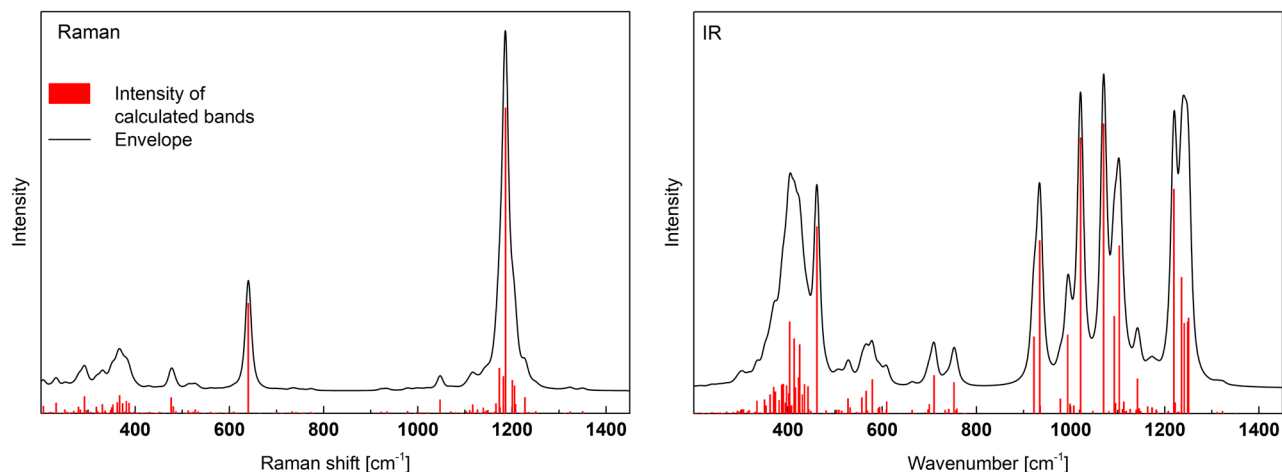
Figure 5. Calculated Raman and IR spectra of B-Al(PO₃)₃.

Frequency (>200) [cm⁻¹]	Intensity Raman (the most intense frequencies [cm⁻¹])	Intensity IR (the most intense frequencies [cm⁻¹])	Assignment to vibrations of Q^i idealized and $P–O_B–P$
<248	Very weak	Very weak	Lattice vibrations and librations
250–617	Weak (292, 367 (s) and 476)	Medium (389, 403 (s), 413, 422, 425, 435, 461 and 579)	Bending (A_1) in $P–O_B–P$ and deformations (bending (A_1) and asymmetric deformations (B_2) of $2(P-O_{NB})$) in Q^2 (Q^2-chains in $[AlO_6]$ environment)
640–777	Medium (640 (s))	Weak (710 (s) and 752)	Symmetric stretching (A_1) in $P–O_B–P$ and bending (A_1) of $2(P-O_{NB})$ in Q^2 (Q^2-chains in $[AlO_6]$ environment)
922–1021	Very weak	Strong (922, 934, 994 and 1021 (s))	Asymmetric stretching (B_1) of $2(P-O_B)$ in Q^2 and asymmetric stretching (B_1) in $P–O_B–P$ (Q^2-chains in $[AlO_6]$ environment)
1047–1149	Very weak (1047 (s))	Strong (1070 (s), 1092, 1103 and 1142)	Symmetric stretching (A_1) of $2(P-O_{NB})$ and symmetric stretching (A_1) of $2(P-O_B)$ in Q^2 (Q^2-chains in $[AlO_6]$ environment)
1159–1186	Very strong (1173, 1182 and 1186 (s))	Very weak	Symmetric stretching (A_1) of $2(P-O_{NB})$ in Q^2 (Q^2-chains in $[AlO_6]$ environment)
1201–1350	Weak (1201 (s), 1206 and 1228)	Strong (1219 (s), 1236, 1241, 1249 and 1250)	Asymmetric stretching (B_1) of $2(P-O_{NB})$ in Q^2 (Q^2-chains in $[AlO_6]$ environment)

Table 2. Calculated Raman and IR active modes of B-Al(PO₃)₃ (more details in the supplementary materials Table S1.2). s—the strongest in range.

The calculated Raman and IR spectra are shown in Fig. 5. Detailed vibration assignments to idealized Q^2 of the C_{2v} point group and their positions are summarized in Table S1.2 (supplementary material) and in simplification in Table 2.

The Raman spectrum of B-Al(PO₃)₃ is characterized by two intense bands. The strongest one is at 1186 cm⁻¹ and weaker at 640 cm⁻¹. The higher frequency band is related to the symmetric stretching vibrations (A_1) of $2(P-O_{NB})$ in the Q^2 structural units. The second lower frequency is due to symmetric stretching (A_1) in $P-O_B-P$ and bending (A_1) of $2(P-O_{NB})$ in Q^2.

The IR spectrum of B-A(PO₃)₃ is more complex. In the range of 922–1350 cm⁻¹, there are three groups of strong bands. The first group between 922 and 1021 cm⁻¹ contains asymmetric stretching vibrations (B_1) of $2(P-O_B)$ in Q^2 and asymmetric stretching (B_1) in $P-O_B-P$. The group between 1047 and 1149 cm⁻¹ is related to the symmetric stretching (A_1) of $2(P-O_{NB})$ and the symmetric stretching (A_1) of $2(P-O_B)$ in Q^2. The last group between 1201 and 1350 cm⁻¹ is due to the asymmetric stretching (B_1) of $2(P-O_{NB})$ in Q^2. The medium intensity in the IR spectrum has vibrations related to bending (A_1) in $P-O_B-P$ and deformations in Q^2 in the range of 250–617 cm⁻¹. Other modes are much weaker.

A-Al(PO₃)₃. The powder XRD diffraction pattern of the synthesized sample containing A-Al(PO₃)₃ is shown in Fig. 6. The Rietveld refinement of the data showed that in the sample two phases can be distinguished. The main crystalline phase is A-Al(PO₃)₃ in a quantity of approximately 99 wt% and the minority phase is an α-cristobalite type of AlPO₄. The detailed composition of the material is given in Table S2.1 (supplementary data). The A-Al(PO₃)₃ crystallizes in a cubic I $\overline{4}$ 3d space group and the fitted basic crystal structure parameter is a = 13.727(6) Å.
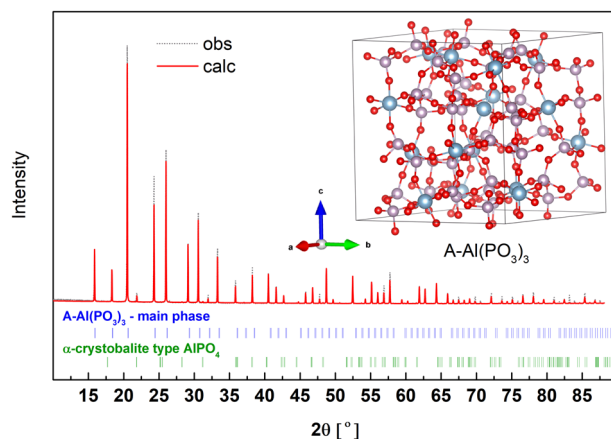
Figure 6. X-ray diffraction pattern (obs) and fit (calc) of A-Al(PO$_3$)$_3$. In the inset, the unit cell of A-Al(PO$_3$)$_3$ with the optimized atoms' positions.
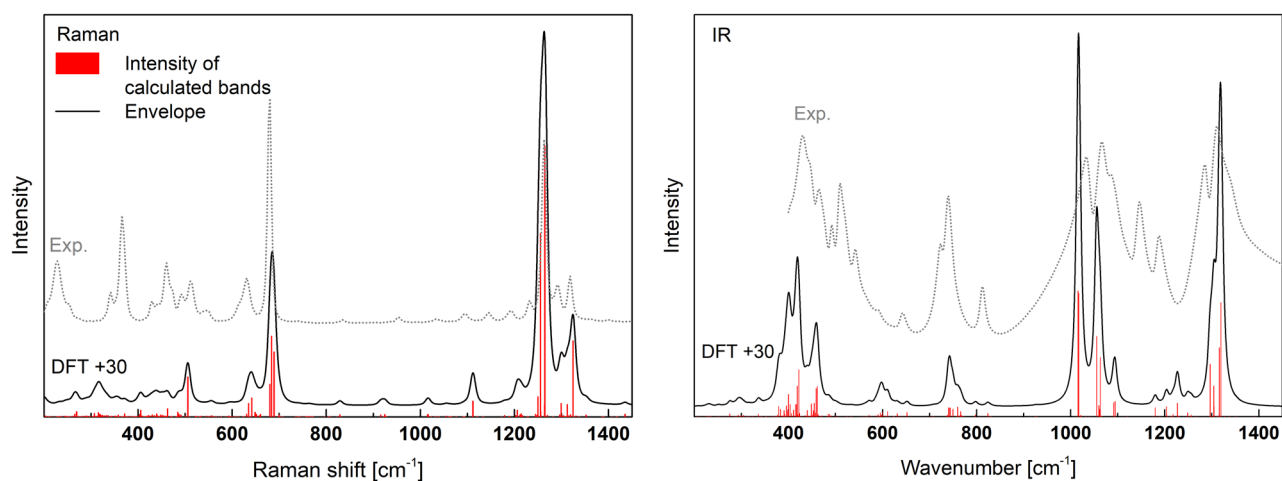

Figure 7. Calculated Raman and IR spectra of A-Al(PO$_3$)$_3$ shifted by + 30 cm^{-1} and experimental IR and Raman spectra (Exp.) of the synthesized material.

In contrast to B-Al(PO$_3$)$_3$ in the A-Al(PO$_3$)$_3$ phase the phosphate network forms 4-membered rings of Q^2 structural units (4Q^2 ring), and the rings are connected by polyhedrons [AlO$_6$]. In this case, the length of the P-O$_B$ bond is in the range of 1.583–1.595 Å, whereas for P-O$_{NB}$ it is in the range of 1.471–1.479 Å. Similarly, as in B-Al(PO$_3$)$_3$ there are no pure double P=O bonds, and all the non-bridging oxygens take part in the formation of P-O$_{NB}$-Al bridges.

The calculated and experimental Raman and IR spectra are presented in Fig. 7. The corresponding vibrations are summarized in detail in Table S1.3 (supp.) and shortened in Table 3. The 4Q^2 rings have S$_4$ space group symmetry and some characteristic vibrations in A-Al(PO$_3$)$_3$ were assigned to this symmetry. It can be seen that there is a very good agreement between the experimental and theoretical results. In both the case of intensities and positions. However, the theoretical spectra were shifted by a constant value of about + 30 cm^{-1} for both Raman and IR results.

The Ramana spectrum of A-Al(PO$_3$)$_3$ has a very strong band at around 1235 cm^{-1} due to the symmetric stretching (A$_1$) of 2(P-O$_{NB}$) in Q^2. The second band of lower intensity at 654 cm^{-1} is related to symmetric stretching (A$_1$) in P–O$_B$–P and bending (A$_1$) of 2(P-O$_{NB}$) in Q^2. In the case of the studied phase, there exist characteristic ring vibrations as presented in Fig. 8. Two bands related to the vibrations at c.a. 1270 cm^{-1} and 1295 cm^{-1}, which is due to asymmetrical and symmetrical vibrations about a fourfold inversion axis of the 4Q^2 ring, respectively. It should be noted that the vibrations are characteristic for A-Al(PO$_3$)$_3$ and are not present in B-Al(PO$_3$)$_3$. Thus, it can be used to distinguish between the two phases.

The IR spectrum has two groups with strong bands at c.a. 886–1046 cm^{-1} and 1283–1405 cm^{-1}. The first group is related to the stretching modes 2(P–O$_B$) in Q^2 and asymmetric stretching (B$_1$) in P–O$_B$–P. The band group 1283–1405 cm^{-1} is related to asymmetric stretching vibrations (B$_1$) of 2(P-O$_{NB}$) in Q^2. The bands related to the bending modes (A1) in P–O$_B$–P and deformations of 2(P-O$_{NB}$)) in Q^2 are in the range of 286–651 cm^{-1} and have a medium intensity. Also, visible in the IR spectra are bands related to symmetric stretching (A$_1$) in P-O$_B$-P and bending (A$_1$) of 2(P-O$_{NB}$) in Q^2 in the range of 654–801 cm^{-1}.

Frequency (> 200) [cm^{-1}]	Intensity Raman (the most intense frequencies [cm^{-1}])	Intensity IR (the most intense frequencies [cm^{-1}])	Assignment to Q^i idealized vibrations and P–O$_B$–P
< 280	Very weak (236, 240 (s) and 277)	Very weak (245 (s))	Lattice vibrations and librations
286–651	Weak (286, 376, 433, 455, 476 (s), 605, 612, 619 and 651)	Medium (370, 389, 392 (s), 419, 429, 431 and 581)	Bending (A$_1$) in P-O$_B$-P and deformations (bending (A$_1$) and asymmetric deformations (B$_2$) of 2(P-O$_{NB}$)) in Q^2 (4Q^2-rings in [AlO$_6$] environment)
654–801	Strong (654 (s) and 659)	Medium (710, 714 and 730 (s))	Symmetric stretching (A$_1$) in P-O$_B$-P and bending (A$_1$) of 2(P-O$_{NB}$) in Q^2 (4Q^2-rings in [AlO$_6$] environment)
886–1046	Very weak (799, 895 and 987 (s))	Strong (986 (s), 1025, 1030 and 1033)	Asymmetric stretching (B$_1$) and symmetric stretching (A$_1$) of 2(P-O$_B$) in Q^2 in different positions and asymmetric stretching (B$_1$) in P-O$_B$-P (4Q^2-rings in [AlO$_6$] environment)
1061–1149	Weak (1082 (s))	Medium (1061, 1064 (s) and 1149)	Symmetric stretching (A$_1$) of 2(P-O$_{NB}$) and symmetric stretching (A$_1$) of 2(P-O$_B$) in Q^2 (4Q^2-rings in [AlO$_6$] environment)
1159–1240	Very strong (1176, 1220, 1226 (r) and 1235 (s))	Weak (1174, 1188, 1197 (s) and 1219)	Symmetric stretching (A$_1$) of 2(P-O$_{NB}$) in Q^2 (4Q^2-rings in [AlO$_6$] environment) and asymmetric vibration about a fourfold inversion axis of 4Q^2 ring
1252–1281	Weak (1270 (r, s))	Medium (1266 (s), 1274 and 1275)	Asymmetric stretching (B$_1$) of 2(P-O$_{NB}$) in Q^2 (4Q^2-rings in [AlO$_6$] environment) and asymmetric vibration about the four-fold inversion axis of 4Q^2 ring
1283–1405	Medium (1283 (r) and 1295 (r, s))	Strong (1286 and 1289 (s))	Asymmetric stretching (B$_1$) of 2(P-O$_{NB}$) in Q^2 (4Q^2-rings in [AlO$_6$] environment) and symmetric vibration about a fourfold inversion axis of the 4Q^2 ring

Table 3. The calculated Raman and IR active modes of A-Al(PO$_3$)$_3$ (more details in the supplementary materials Table S1.3). r—frequency assigned to the 4Q^2 ring, s—the strongest in range.
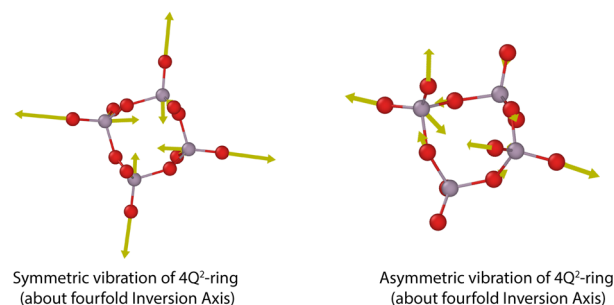

Symmetric vibration of 4Q^2-ring
(about fourfold Inversion Axis)

Asymmetric vibration of 4Q^2-ring
(about fourfold Inversion Axis)

Figure 8. Examples of vibrations of 4Q^2-rings in A-Al(PO$_3$)$_3$.

Aluminum cyclohexaphosphate—Al(PO$_3$)$_3$. Another polymorphic form of Al(PO$_3$)$_3$ is aluminum cyclohexaphosphate. The powder X-ray diffraction pattern of the synthesized material is shown in Fig. 9. According to the Rietveld analysis, the assumed phase is the main (c.a. 85 wt%) and the rest is A-Al(PO$_3$)$_3$. The detailed phase composition of the material is summarized in Table S2.2 (supp.). The main phase crystallizes in a monoclinic P12$_1$/c1 space group and the fitted crystal structure parameters are a=6.072(2) Å, b = 15.036(1) Å, c = 8.182(9) Å, β = 105.12°.

The crystal structure of the aluminum cyclohexaphosphate Al(PO$_3$)$_3$ is similar to A-Al(PO$_3$)$_3$ built of rings that, on the contrary, are composed of 6Q^2 units connected by [AlO$_6$] octahedra. In this case, the length of the P-O$_B$ bond is in the range of 1.581–1.598 Å, whereas for P-O$_{NB}$ it is in the range of 1.475–1.488 Å.

The calculated and experimental Raman and IR spectra are presented in Fig. 10. The corresponding vibrations are summarized in detail in Table S1.4 (supp.) and shortened in Table 4. The 6Q^2 rings have C$_i$ space-group symmetry and some characteristic vibrations were assigned to this symmetry. Similarly to previously, there is good agreement between the experimental and theoretical results. The best convergence is obtained when the theoretical spectrum is shifted by the constant value of c.a. + 25 cm^{-1}.

The Raman spectrum of aluminum cyclohexaphosphate is similar to those of A-Al(PO$_3$)$_3$ and B-Al(PO$_3$)$_3$. The strongest band is related to the symmetric stretching modes (A$_1$) of 2(P-O$_{NB}$) in Q^2. The position of the band is c.a. 1215 cm^{-1}. The second strong band is at c.a. 715 cm^{-1} and is due to symmetric stretching vibrations (A$_1$) in P-O$_B$-P and bending modes (A$_1$) of 2(P-O$_{NB}$) in Q^2. There are also characteristic 6Q^2-ring modes active like symmetric vibrations A$_g$ (Fig. 11) in the range of 1121–1341 cm^{-1} and 561 cm^{-1}.

In the IR spectrum, the strongest vibrations are in the range of 883–1082 and 1222–1341 cm^{-1}. The first group is related to the stretching of 2(P–O$_B$) Q^2 and the asymmetric stretching (B$_1$) in P–O$_B$–P. The second group is
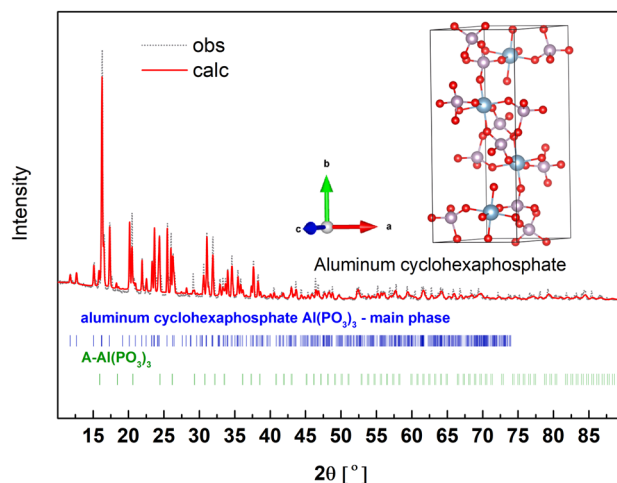
Figure 9. X-ray diffraction pattern (obs) and the fitted (calc) of aluminum cyclohexaphosphate -Al(PO$_3$)$_3$. In the inset, the unit cell of the compound with the optimized atom positions.
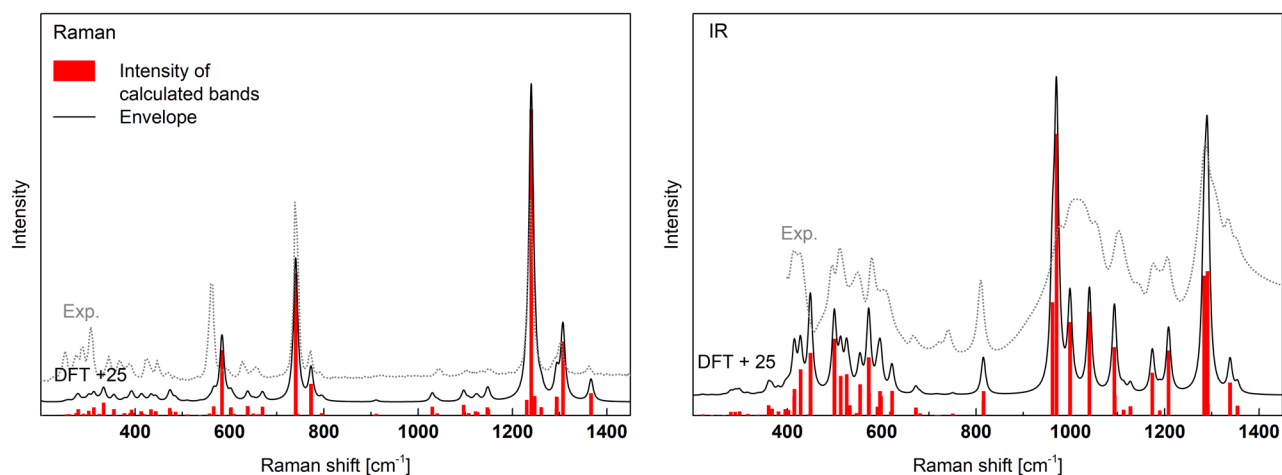

Figure 10. Calculated Raman and IR spectra of aluminum cyclohexaphosphate -Al(PO$_3$)$_3$ shifted by +25 cm^{-1} and experimental IR and Raman spectra (Exp.) of the synthesized material.

related to the asymmetric stretching (B$_1$) of 2(P-O$_{NB}$) in Q^2. Good visible vibrations in the range 1088–1215 cm^{-1} are related to the asymmetric A$_u$ vibration of the 6Q^2-ring (Fig. 11).

NaAlP$_2$O$_7$. In Al$_2$O$_3$-P$_2$O$_5$ there is no known pure compound containing Q^1 structural units. Therefore, sodium-containing NaAlP$_2$O$_7$ was chosen where the unit cell is built of Q^1–Q^1 dimers. The XRD pattern of the synthesized material is presented in Fig. 12. The main crystal phase present in the obtained material is NaAlP$_2$O$_7$ (c.a. 85 wt%). Secondary minor phases are AlPO$_4$ of the berlinite and cristobalite type and Al$_2$O$_3$. The detailed phase composition is given in Table S2.3 (suppl.). The main phase crystallizes in a monoclinic P12$_1$/c1 space group and the fitted crystal structure parameters are $a = 7.197(4)$ Å, $b = 7.704(5)$ Å, $c = 9.314(5)$ Å, $\beta = 111.72(5)°$.

In the unit cell Q^1-Q^1 (P$_2$O$_7$) dimers are connected to [AlO$_6$] octahedra and sodium polyhedra. In this case, the distance of P-O$_B$ is in the range of 1.612–1.616 Å and P-O$_{NB}$ in the range of 1.499–1.527 Å. The excess of the P positive charge is now redistributed over 3 non-bridging oxygens in the Q^1 unit. Because the unit has only one bond longer (P–O$_B$) and three of similar lengths (P–O$_{NB}$), the idealized symmetry of the unit is the same as the Q^3 unit. Thus, Q^1 has the same C$_{3v}$ point group as Q^3.

The calculated and measured Raman and IR spectra are presented in Fig. 13. Good agreement is also observed between the theory and the experiment. The best results may be obtained after including about +40 cm^{-1} shift of the theoretical spectra. The detailed positions and intensity of the calculated active bands are summarized in the supp. (Table S1.5), and in the simplified form in Table 5.

The most intense band in the Raman spectrum is at 1055 cm^{-1} related to the symmetric stretching (A$_1$) modes of 3(P–O$_{NB}$) in Q^1. With this feature are associated bands of higher frequencies in the range of 1073–1251 cm^{-1} related to asymmetric stretching modes (E) of 3(P–O$_{NB}$) in Q^1. However, the intensity of the asymmetric vibrations

Frequency (> 200) [cm^{-1}]	Intensity Raman (the most intense frequencies [cm^{-1}])	Intensity IR (the most intense frequencies [cm^{-1}])	Assignment to Q^i idealized vibrations and P–O$_B$–P
< 260	Very weak	Very weak	Lattice vibrations and librations
265–555	Very weak (287, 308 (s), 448 and 541)	Medium (389, 402, 423, 474 (s), 488, 500, 529 and 547)	Bending (A$_1$) in P-O$_B$-P and deformations (bending (A$_1$) and asymmetric deformations (B$_2$) of 2(P-O$_{NB}$)) in Q^2 (6Q^2-rings in [AlO$_6$] environment)
559 (r)	Medium	Nonactive	Twisting (A$_2$) of 2(P-O$_{NB}$) and 2(P-O$_B$) in Q^2 (6Q^2-rings in [AlO$_6$] environment) and symmetric A$_g$ vibration of 6Q^2 molecule
565–656	Weak (578, 613 (s) and 645)	Medium	
(571 and 597 (s))	Bending (A$_1$) in P-O$_B$-P and deformations (bending (A$_1$) and asymmetric deformations (B$_2$) of 2(P-O$_{NB}$)) in Q^2 (6Q^2-rings in [AlO$_6$] environment)		
690–791	Strong (715 (s) and 748)	Weak (791(s))	Symmetric stretching (A1) in P-O$_B$-P and bending (A$_1$) of 2(P-O$_{NB}$) in Q^2 (6Q^2-rings in [AlO$_6$] environment)
883–1082	Weak (1005 and 1071 (s))	Strong (937, 946 (s), 974, 1015 and 1068)	Symmetric (A$_1$) and asymmetric (B$_1$) stretching of 2(P-O$_B$) in different Q^2 positions and asymmetric stretching (B$_1$) in P-O$_B$-P (6Q^2-rings in [AlO$_6$] environment)
1088–1215	VERY strong (1121 (r), 1205 (r, s) and 1215 (r))	Medium (1149 (r) and 1183 (r, s))	Symmetric stretching (A$_1$) of 2(P-O$_{NB}$) in the Q^2 (6Q^2-rings in [AlO$_6$] environment) and Symmetric (Raman spectra) A$_g$ and asymmetric (IR spectra) A$_u$ vibration of 6Q^2 molecule
1222–1341	Medium (1222 (r), 1236 (r), 1268 (r), 1282 (r) and 1341 (r, s))	Strong (1259, 1265 (s) and 1314)	Asymmetric stretching (B$_1$) of 2(P-O$_{NB}$) in Q^2 (6Q^2-rings in [AlO$_6$] environment) and symmetric A$_g$ vibration of 6Q^2 molecule

Table 4. The calculated Raman and IR active modes of aluminum cyclohexaphosphate -Al(PO3)3 (more details in the supplementary materials Table S1.4). r—frequency assigned to the 6Q^2 ring, s—the strongest in the range.
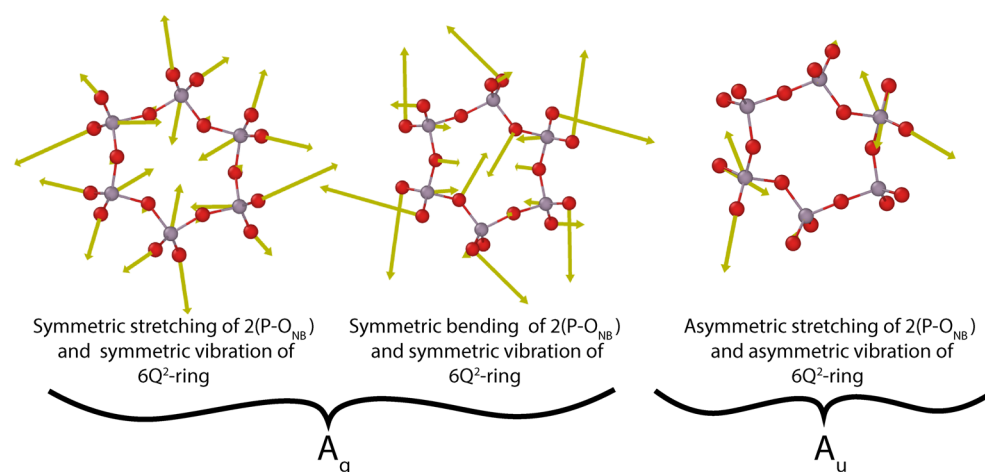

Figure 11. Examples of vibrations of 6Q^2-ring in aluminum cyclohexaphosphate -Al(PO$_3$)$_3$.

is considerably lower. The second strong band is at 737 cm^{-1} due to symmetric stretching (A$_1$) in P–O$_B$–P and symmetric deformation (A1) of 3(P–O$_{NB}$).

The IR spectrum is characterized by two strong groups of bands. The first in the range of 892–921 cm^{-1} is related to asymmetric stretching vibrations (B$_1$) of P–O$_B$–P. The second in the range of 1073–1251 cm^{-1} is related to the asymmetric stretching modes (E) of 3(P–O$_{NB}$) in Q^1. The medium strength has bands related to bending (A$_1$) in P–O$_B$–P, asymmetric deformation (E) of 3(P–O$_{NB}$), and symmetric stretching (A$_1$) of 3(P–O$_{NB}$) (see Table 5).

α-Cristobalite type AlPO$_4$. The powder XRD diffraction pattern of the cristobalite type of AlPO$_4$ is presented in Fig. 14. In this case, we were unable to obtain the pure phase. The main crystalline compound was assumed to be AlPO$_4$ (c.a. 67 wt%). The rest of the crystalline phases in the sample are Al$_2$O$_3$ (c.a. 16 wt%) with the minor addition of A-Al(PO$_3$)$_3$ and the berlinite type of AlPO$_4$. The detailed phase composition and the quan-
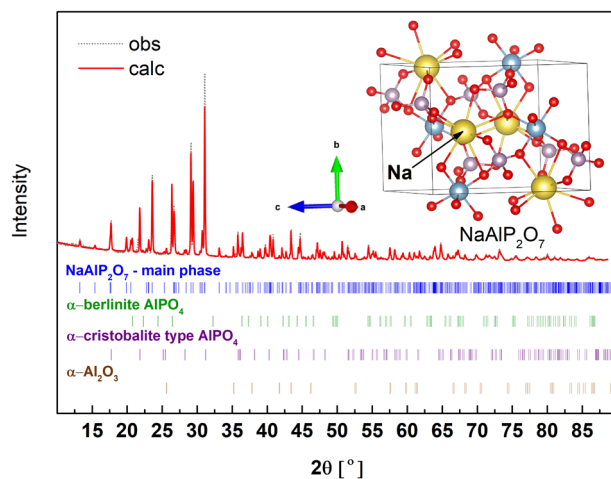
Figure 12. X-ray diffraction pattern (obs) and fit (calc) of $NaAlP_2O_7$. Inset, the unit cell of the compound with the optimized atom positions.
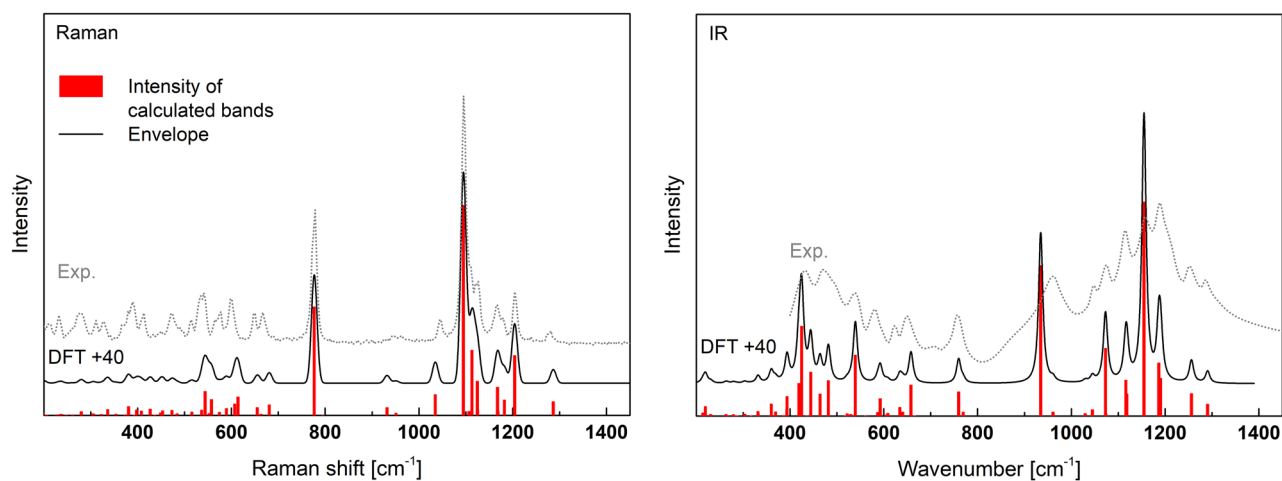

Figure 13. Calculated Raman and IR spectra of $NaAlP_2O_7$ shifted by $+40$ cm^{-1} and experimental Raman and IR spectra (Exp.) of the synthesized material.

Frequency (>200) [cm^{-1}]	Intensity Raman (the most intense frequencies [cm^{-1}])	Intensity IR (the most intense frequencies [cm^{-1}])	Assignment to Q^i idealized vibrations and $P-O_B-P$
<330	Very weak	Very weak	Lattice vibrations and librations
341–641	Weak (341, 504 (s), 518, 567, 574 and 641)	Medium (354, 379, 385 (s), 404, 424, 442, 499, 552 and 618)	Bending (A_1) in $P-O_B-P$ and Asymmetric (E) deformation of $3(P-O_{NB})$ in Q^1 (in [AlO_6] and Na^+ environment)
720–755	Strong (737 (s))	Weak (720 (s))	Symmetric stretching (A_1) in $P-O_B-P$ and symmetric deformation (A1) of $3(P-O_{NB})$ in Q^1 (in the [AlO_6] and Na^+ environment)
892–921	Very weak (895 (s))	Strong	Asymmetric stretching (B_1) in $P-O_B-P$ (in [AlO_6] and Na^+ environment)
990–1067	Very strong (1055 (s))	Medium (1033 (s))	Symmetric stretching (A_1) of $3(P-O_{NB})$ in Q^1 (in [AlO_6] and Na^+ environment)
1073–1251	Medium (1073 (s), 1085, 1128, 1142, 1164 and 1247)	Strong (1076, 1115 (s), 1147, 1151 and 1216)	Asymmetric stretching (E) of $3(P-O_{NB})$ in Q^1 (in [AlO_6] and Na^+ environment)

Table 5. The calculated Raman and IR active modes of $NaAlP_2O_7$ (more details in the supplementary material Table S1.5). s—the strongest in range.
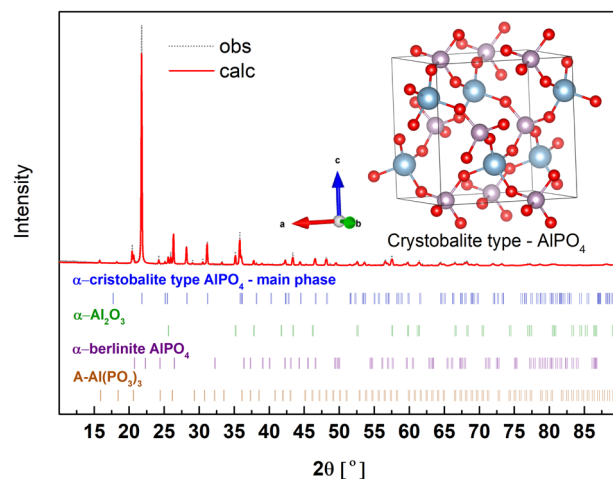
Figure 14. X-ray diffraction pattern (obs) and the fitted (calc) of α-cristobalite type AlPO$_4$. Inset, the unit cell of the compound with the optimized atom positions.
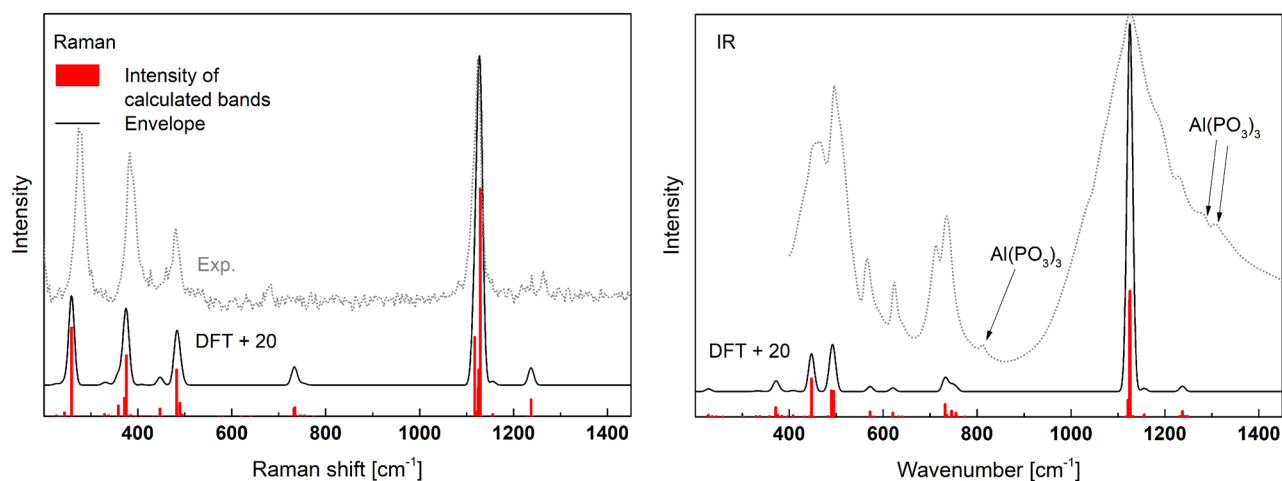

Figure 15. Calculated Raman and IR spectra of α-cristobalite type AlPO$_4$ shifted by +20 cm^{-1} and experimental IR and Raman spectra (Exp.) of the synthesized material.

tified analysis are summarized in Table S2.4 (supp.). The main phase crystallizes in a orthorombic C222$_1$ space group and the fitted crystal structure parameters are $a = 7.103(4)$ Å, $b = 7.096(3)$ Å, $c = 7.011(5)$ Å.

The α-cristobalite type AlPO$_4$ is built of Q^0 structural units connected by [AlO$_4$] tetrahedra. In the crystal structure, there are no bridging oxygen atoms, and all the oxygens are non-bridging. The length of the P-O$_{NB}$ bond is in the range of 1.521–1.523 Å. Due to the fact that all oxygens in the [PO$_4$] tetrahedrons have a similar P-O distance, the tetrahedron is close to ideal and can be described by symmetry of the T$_d$ point group.

The calculated and experimental Raman and IR spectra of the samples are presented in Fig. 15. The material obtained is polyphase in the case where characteristic vibrations of A-Al(PO$_3$)$_3$ were also detected in the IR spectra. On the other hand, Raman spectroscopy is measured at a point, and it was possible to detect the spectrum of the pure cristobalite phase. In this case, good agreement between theory and experiment can also be evidenced. The best results were obtained when the calculated spectra had been shifted to a value of +20 cm^{-1}. A detailed description of the active modes is given in Table S1.6 (supp.) and the simplified version in Table 6.

The Raman spectrum is characterized by a strong band at 1109 cm^{-1} due to symmetric stretching vibrations (A$_1$) in Q^0. In the spectrum there are also visible 3 characteristic bands in the range of 239–735 cm^{-1}. The two in the range of 325–735 cm^{-1} are related to the symmetric bending (E) and asymmetric deformation (F$_2$) modes of Q^0. The band 239 cm^{-1} is due to lattice vibrations.

The most characteristic feature of the IR spectrum is a strong band at 1106 cm^{-1} that may be assigned to asymmetric stretching modes (F$_2$) in Q^0. Also, in the IR spectra there are good visible medium vibrations related to symmetric bending (E) of Q^0 and weak vibrations related to asymmetric deformation (F$_2$) of Q^0.

α-Berlinite AlPO$_4$. The next polymorphic form of AlPO$_4$ is the berlinite type. The XRD pattern of the synthesized material is given in Fig. 16. As can be seen, the synthesized material was polyphase. The main crystalline

Frequency (> 200) [cm⁻¹]	Intensity Raman (the most intense frequencies [cm⁻¹])	Intensity IR (the most intense frequencies [cm⁻¹])	Assignment to Q^i idealized vibrations and P–O$_B$–P
< 239	Medium (239 (s))	Very weak	Lattice vibrations and librations
309–365	Medium (356 (s))	Medium (351 (s))	Symmetric bending (E) of Q^0 (in [AlO$_4$] environment)
476–735	Medium (462 (s))	Weak (428 (s), 470 and 475)	Asymmetric deformation (F$_2$) of Q^0 (in [AlO$_4$] environment)
1097–1106	Medium (1097 (s) and 1106)	Very strong (1102 and 1106 (s))	Asymmetric stretching (F$_2$) of Q^0 (in [AlO$_4$] environment)
1109	Very strong	Very weak	Symmetric stretching (A$_1$) of Q^0 (in [AlO$_4$] environment)
1112–1217	Very weak (1217 (s))	Very weak (1217 (s))	Asymmetric stretching (F$_2$) of Q^0 (in [AlO$_4$] environment)

Table 6. The calculated Raman and IR active modes of α-cristobalite type AlPO$_4$ (more details in the supplementary materials Table S1.6). S—the strongest in range.
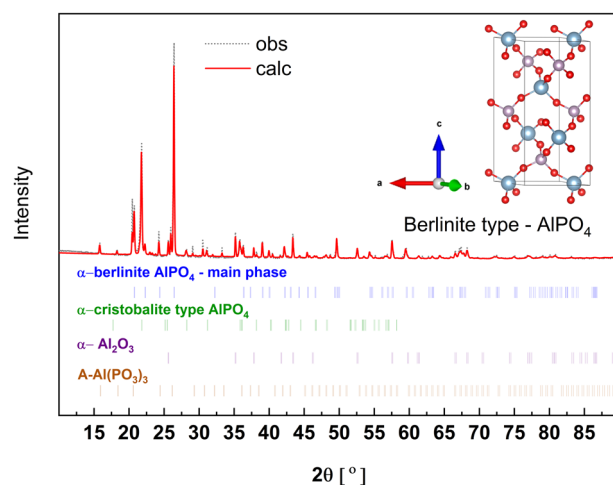

Figure 16. X-ray diffraction pattern (obs) and the fitted (calc) of α-berlinite type AlPO$_4$. Inset, the unit cell of the compound with the optimized atom positions.

compound is the assumed berlinite type of AlPO$_4$ (c.a. 57 wt%). There are also Al$_2$O$_3$, A-Al(PO$_3$)$_3$, and other polymorphic phase of AlPO$_4$ such as cristobalite. The detailed phase composition of the synthesized sample is summarized in Table S2.5 (supp.). The main phase crystallizes in a trigonal P3$_2$21 space group and the fitted crystal structure parameters are a = b = 4.948(5) Å, c = 10.950(7) Å.

The crystal structure of berlinite is very similar to that of cristobalite AlPO$_4$. The unit cell is composed of Q^0 structural units connected by [AlO$_4$] tetrahedra with the P-O$_B$ distance in the range of 1.507–1.512 Å.

The calculated and experimental Raman and IR spectra are shown in Fig. 17. In this case, the best agreement is obtained for the theoretical data shifted by + 25 cm⁻¹. Similarly to the above, the most suitable Raman spectrum was chosen to compare with the calculated spectra. In the IR spectrum, in addition to bands related to α-cristobalite type AlPO$_4$ there are weak bands of A-Al(PO$_3$)$_3$. The detailed Raman and IR active modes with the proper assignment are given in Table S1.7 (supp.) and the simplified in Table 7.

On the Raman spectrum, the strongest band at 1109 cm⁻¹ may be assigned to vibrations of symmetric stretching (A1) in Q^0. The position of this band is very similar in α-cristobalite type AlPO$_4$ and α-berlinite. The medium bands are present in the range of 451–741 cm⁻¹ and are related to the symmetric bending modes (E) of Q^0. The bands related to the asymmetric deformation (F$_2$) of Q^0 are very weak in the α-berlinite spectrum.

On the IR spectrum, the strongest band is at 1092 cm⁻¹ due to asymmetric stretching vibrations (F$_2$) in Q^0. Furthermore, bands in the range of 451–741 cm⁻¹ related to asymmetric deformation (F$_2$) of Q^0 are clearly visible in the spectrum.

Discussion

Analyzing the obtained experimental and theoretical results one may see that the main intense bands are due to P-O bonds vibrations in Q^i structural units in the higher frequency range and P-O-P in the midregion. This is the most well seen in the case of the Raman spectra, wherein in the most considered cases the two bands are dominating. The intensity of the midband decreases with the Q^i index, which is related to the decrease of the number of P–O–P linkages. The position of the symmetric modes is centered at frequencies lower than asymmetric.
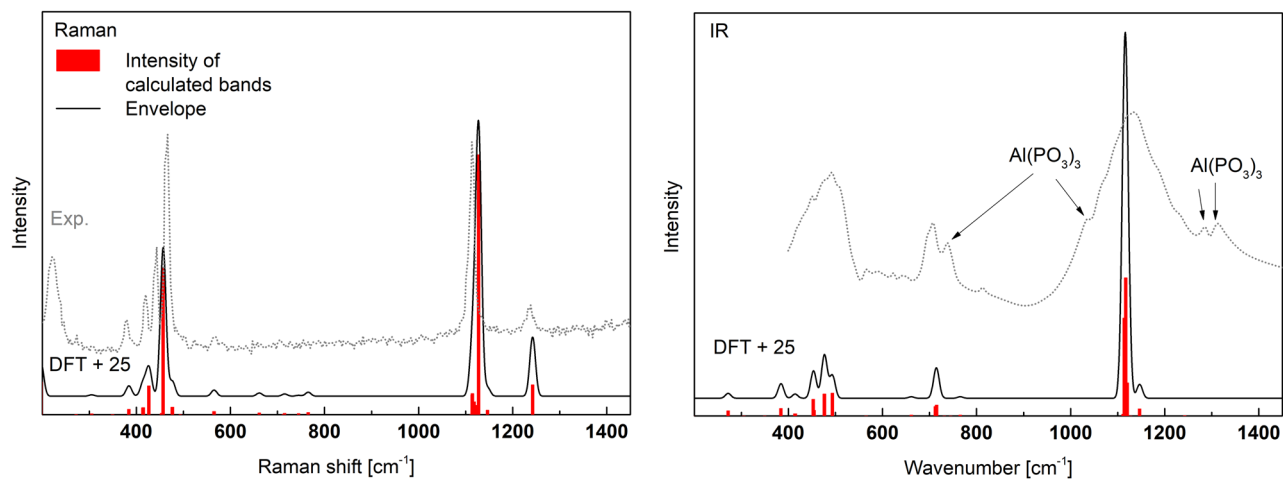
Figure 17. Calculated Raman and IR spectra of α-berlinite type $AlPO_4$ shifted by $+20$ cm^{-1} and experimental IR and Raman spectra (Exp.) of the synthesized material.

Frequency (>200) [cm^{-1}]	Intensity Raman (the most intense frequencies [cm^{-1}])	Intensity IR (the most intense frequencies [cm^{-1}])	Assignment to Q^i idealized vibrations and P–O_B–P
< 280	Very weak	Very weak	Lattice vibrations and librations
325–432	Medium (389, 402 and 432 (s))	Weak (428 (s))	Symmetric bending (E) of Q^0 (in [AlO_4] environment)
451–741	Very weak	Medium (451 (s), 469 and 690)	Asymmetric deformation (F_2) of Q^0 (in [AlO_4] environment)
1087–1095	Weak (1089 (s))	Very strong (1089, 1092 (s) and 1095)	Asymmetric stretching (F_2) of Q^0 (in [AlO_4] environment)
1103–1122	Very strong (1103 (s))		Symmetric stretching (A_1) of Q^0 (in [AlO_4] environment)
1217	Weak	Very weak	Asymmetric stretching (F_2) of Q^0 (in [AlO_4] environment)

Table 7. The calculated Raman and IR active modes of α-berlinite type $AlPO_4$ (more details in the supplementary materials Table S1.7). S—the strongest in range.
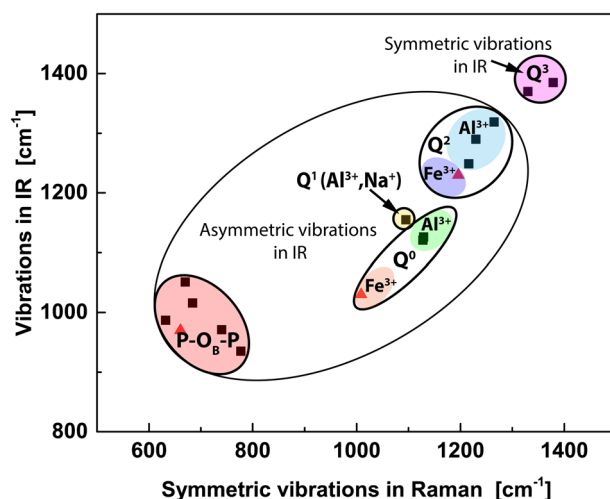

Figure 18. The most intense bands positions of symmetric and asymmetric stretching vibrations of P-O_{NB} in Q^i and P-O_B-P in Raman and IR spectra. Al^{3+}- vibrations in aluminum phosphates, (Al^{3+},Na^+) in $NaAl(P_2O_7)$ and Fe^{3+} in iron phosphates. Data in red triangles from[42–44].

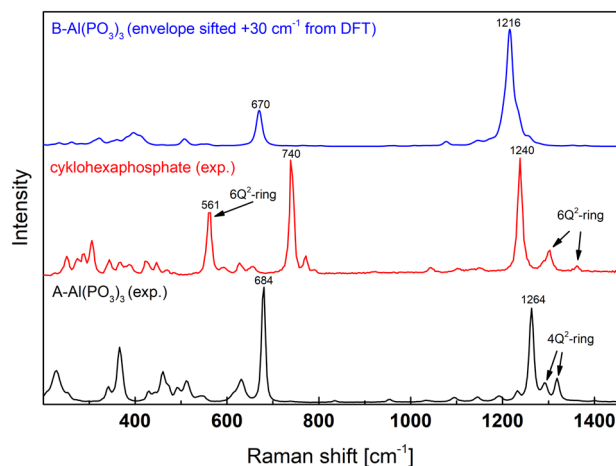**Figure 19.** Comparison of experimental spectra of $Al(PO_3)_3$ polymorphs and envelope of calculated spectra of B-$Al(PO_3)_3$. The characteristic bands for the $6Q^2$-ring and the $4Q^2$-ring were marked in the figure.

The position of the bands related to Q^i units depends on the value of the parameter i, and with the parameter increase the position shifts towards higher values, which is presented in Fig. 18. The separated ranges of the vibrations for specific Q^i spices can be distinguished. This shows that Raman and IR spectroscopies may provide important information concerning the Q^i distribution in materials.

On the other hand, the modes related to the different vibrations in $[AlO_x]$ polyhedrons are very weak, and it seems that spectroscopies cannot be utilized to distinguish the Al-O environment. However, it should be notated that the occurrence of polyhedrons influence the position of the vibrations of Q^i units as shown in Fig. 18. Comparing the results with the data summarized in[42–44] with respect to iron phosphates, it can be detected that Al^{3+} shifts the Q^i vibration toward higher frequencies compared to Fe^{3+}. This may be useful in the case of materials containing iron and aluminum to differentiate Q^i species connected with Al^{3+} and Fe^{3+} cations as in glasses. The position of the band related to the symmetric stretching modes of $3(P-O_{NB})$ in the structural unit of $NaAlP_2O_7$ is very close to the band in Q^0 (α-cristobalite or α-berlinite). The position of this band for Q^1 is usually higher than Q0 [19, 48]. The ionic nature of Na^+ shifts the band toward lower values. A similar effect can be detected for Fe and Al, and iron, which is more ionic to oxygen than aluminum, also lowers the position of the band in Q^i species[19,42,45,46].

Another important observation is evidence of mid-intensity bands characteristic of phosphate rings vibrations in $Al(PO_3)_3$. The vibrations are located at higher frequencies next to the most intense band (Fig. 19). The bands characteristic to $6Q^2$- and $4Q^2$-rings are well visible and allow to distinguish between different $Al(PO_3)_3$ polymorphic forms.

Additionally, the main intense band for the ring structures is shifted toward the higher values, and the shift is the highest for the $4Q^2$-rings. The shift is probably related to the increase in the stiffness of bonds in ring structures. The rings are more rigid than the chains, and the smaller rings are more rigid than the larger ones. Therefore, the position moves to a higher frequency.

Conclusions

Theoretical Ramana and IR spectra of aluminum phosphate compounds containing Q^i structural units were calculated from Q^0 to Q^3 and characteristic vibration modes were described. The selected compounds were synthesized, and the experimental spectra were compared with those of theoretical. It was evidenced by the good agreement between the theoretical and experimental results. The best convergence was obtained when the calculated Ramana and IR spectra were shifted in the range of $+20-+40$ cm^{-1} without applying any scaling factor.

It was evidenced that the Raman spectra are characterized by the presence of two characteristic bands in the mid-and high-frequency ranges. The mid-band is originating from P–O–P bridges, whereas the higher band is the result of P–O vibrations in Q^i tetrahedrons. The position of the high-frequency band is correlated with the index i in the Q^i species and can be used to predict the distribution of Q^i units in materials.

In the case of the Raman spectra, symmetric vibrations are much more intense than asymmetric, whereas in the case of the IR the opposite effect is evidenced. The IR spectra are also dominated by two bands because of the vibrations of P-O-P and P-O in Q^i units, similar to Raman.

For $Al(PO_3)_3$ and $AlPO_4$ differences in Raman spectra related to different polymorphic forms were observed and described.

Materials and methods

Simulations. Calculations of Raman and IR spectra were conducted for the crystalline compounds presented in Table 8 using Quantum Espresso 6.4 software[47]. In the calculation procedure, the unit cell parameter was taken from the reference, and the positions of the atoms were optimized. The unit cell parameters were not

Crystalline compound	Crystal system	Symmetry space group name in Hermann–Mauguin notation	Phosphate structural unit in crystalline compound (Q^i notation)	Unit cell parameters: a, b, c [Å] α, β, γ [°]	Source, COD database ID
o'-P_2O_5	Orthorhombic	P n m a	Q^3	9.193, 4.890, 7.162 $\alpha=\beta=\gamma=90$	[25], 2,003,536
B-Al(PO$_3$)$_3$	Monoclinic	I 1 c 1	Q^2 (chains)	10.423, 18.687, 9.222 $\alpha=\gamma=90$, $\beta=81.630$	[26], 2,106,619
A-Al(PO$_3$)$_3$	Cubic	I $\bar{4}$ 3 d	Q^2 (4 membered rings)	a = b = c = 13.63 $\alpha=\beta=\gamma=90$	[27], 1,010,266
Aluminum cyclohexaphosphate-Al(PO$_3$)$_3$	Monoclinic	P 1 2$_1$/c 1	Q^2 (6 membered rings)	6.093, 15.068, 8.202 $\alpha=\gamma=90$, $\beta=105.166$	[28], 2,225,399
NaAl(P$_2$O$_7$)	Monoclinic	P 1 2$_1$/c 1	Q^1	7.203, 7.710, 9.326 $\alpha=\gamma=90$, $\beta=111.743$	[48], 8,103,838
α-Cristobalite type AlPO$_4$	Orthorhombic	C 2 2 2$_1$	Q^0	7.084, 7.082, 6.999 $\alpha=\beta=\gamma=90$	[31], 1,532,548
α-Berlinite (AlPO$_4$)	Trigonal	P 3$_2$ 2 1	Q^0	a = b = 4.944, c = 10.950 $\alpha=\beta=90$, $\gamma=120$	[33], 9,006,404

Table 8. Calculated and synthesized crystalline compounds.

Expected crystalline compound at room temperature:	Synthesis temperature [°C]
A-Al(PO$_3$)$_3$	900
Aluminum cyclohexaphosphate Al(PO$_3$)$_3$	550
NaAlP$_2$O$_7$	850
α-Cristobalite type AlPO$_4$	1050
α-Berlinite (AlPO$_4$)	750

Table 9. Synthesis temperatures of crystalline compounds.

optimized to decrease the calculation time, especially for the big unit cells. This approach may limit the accuracy of the results. Nevertheless, most of the predicted spectra are compared to the experimental or literature data to validate the calculation procedure.

The PWscf program included in the Quantum Espresso package was used to optimize positions and perform self-consistent field SCF calculations. This program is based on Density Functional Theory (DFT), a plane-wave basis set, and pseudopotentials. The local density approximation LDA and optimized norm-conserving Vanderbilt scalar relativistic pseudopotentials from the Pseudo Dojo project[49,50] were used in the calculations. The cut-off energy for valence electrons plane-waves basis set and charge densities were 50 and 200 Ry, respectively. The Monkhorst–Pack k-point sampling scheme with a $3\times3\times3$ mesh grid was used. Self-consistency and convergence of total energy for ionic minimization were set to 10^{-8} and 10^{-4} Ry, respectively. The results of the SCF calculations for optimized structures of crystalline compounds were used in Raman and IR spectra calculations. The calculations of Raman and IR spectra were performed using the PHonon program from the Quantum Espresso package which is based on density functional perturbation theory (DFPT). The k-point grid remained the same as in the previous calculations. The threshold for self-consistency was set at 10^{-12} Ry. The selected k-point mesh was sufficient to obtain satisfactory results and at the same time a decent calculation time. To better visualize IR and Raman theoretical spectrum, the envelopes were calculated by a script written in Python using SciPy library[51].

Synthesis. Crystalline compounds included in Table 8 were synthesized, except o'-P_2O_5 and B-Al(PO$_3$)$_3$. Stoichiometric quantities of chemically pure NH$_4$H$_2$PO$_4$, Al$_2$O$_3$, and Na$_2$CO$_3$ were used. The synthesis was conducted according to the following procedure. The starting NH$_4$H$_2$PO$_4$ was decomposed into H$_3$PO$_4$ by heating to 200 °C in a Al$_2$O$_3$ crucible in an electric furnace. The H$_3$PO$_4$ obtained was kept at 200 °C for 2 h. The molten H$_3$PO$_4$ was thoroughly mixed with Al$_2$O$_3$ or/and Na$_2$CO$_3$. The resulting pastes were placed in an alumina combustion boat. The samples were sintered according to the temperatures in Table 9. Synthesis temperatures were selected according to[4,11,28]. Due to the high hygroscopicity of P$_2$O$_5$, it must be synthesized in tightly closed containers. Also, the measurement procedure using XRD, Raman, or IR spectroscopy must be performed in the absence of air[25]. The synthesis of o'-P$_2$O$_5$ has been ongoing for several weeks. Due to these difficulties, it was decided to abandon the synthesis of o'-P$_2$O$_5$. B-Al(PO$_3$)$_3$ was not obtained from molten H$_3$PO$_4$ and Al$_2$O$_3$ at temperatures of 550 and 900 °C. A synthesis at 700 °C was also performed and a small amount of B-Al(PO$_3$)$_3$ is present in the sample but not enough to compare with the calculated spectra. This sample contains mainly A-Al(PO$_3$)$_3$ (Raman and IR spectra in the supplementary materials Fig. S2.1 and Fig. S2.2). Obtaining B-Al(PO$_3$)$_3$ from melting Al$_2$O$_3$ with HPO$_3$ has been reported[26]. Also, in[30] V. Bemmer et al. report only aluminum cyclohexaphosphate or/and A-Al(PO$_3$)$_3$ obtained from H$_3$PO$_4$ with various precursors (Al(OH)$_3$, Al(NO$_3$)$_3$ or AlCl$_3$) water solutions at temperatures 500 °C and 800 °C.

All of the steps of the synthesis were performed in an air atmosphere. The samples were gradually heated to the synthesis temperature for 5 h and then kept at the temperature for 8 h. Then were cooled to room temperature

with the furnace. The obtained materials were visibly porous as a result of the release of water vapor during synthesis. The samples were then removed from the containers and crushed into smaller pieces. After berlinite synthesis, the part of Al_2O_3 did not react. Therefore, the sample was ground in an agate mortar and powder was pressed into a tablet using a hydraulic press. The pressed sample was sintered at 750 °C for 8 days.

The crystalline compositions of the samples were checked using XRD. Powder XRD measurements were carried out with a Philips X'Pert Pro diffractometer and Cu $K_{\alpha 1}$ radiation. The phase compositions of the obtained materials and the crystal structure parameters have been obtained using the Rietveld method using GSAS-II software[52].

All Raman measurements were made using a Witec Alpha 300 M + Confocal Raman Imaging system with the application of a 50 × air objective (Zeiss, LD EC Epiplan-Neofluar, NA = 0.55). The spectrometer was equipped with an air-cooled solid-state laser operating at 488 nm, a CCD detector that was cooled to − 60 °C, and 600 grooves per mm of gratings. Raman spectra of each sample were collected with two scans and an integration time of 20 s.

Spectroscopic studies were carried out in middle infrared (MIR) regions (4000–400 cm^{-1}) using a Fourier transformation spectrometer (FT-IR). Samples were prepared using tablet methods in KBr. Measurements were collected after 128 scans at a resolution of 4 cm^{-1}.

Data availability
The datasets generated during and/or analysed during the current study are available from the corresponding author on reasonable request.

References

1. Wagh, A. S. Aluminum phosphate ceramics. In *Chemically Bonded Phosphate Ceramics* 141–155 (Elsevier, 2016). doi:https://doi.org/10.1016/B978-0-08-100380-0.00011-7.
2. Kominami, H., Matsuo, K. & Kera, Y. Crystallization and transformation of aluminum orthophosphates in organic solvent containing a small amount of water. *J. Am. Ceram. Soc.* **79**, 2506–2508. https://doi.org/10.1111/j.1151-2916.1996.tb09008.x (1996).
3. Roy, A. K. & Sircar, N. R. A study of the clay-phosphoric acid system by thermal analysis. *Trans. Indian Ceram. Soc.* **41**, 101–104. https://doi.org/10.1080/0371750X.1982.10822584 (1982).
4. Morris, J. H., Perkins, P. G., Rose, A. E. A. & Smith, W. E. The chemistry and binding properties of aluminium phosphates. *Chem. Soc. Rev.* **6**, 173. https://doi.org/10.1039/cs9770600173 (1977).
5. Zhuravleva, P. L., Kitaeva, N. S., Shiryakina, Y. M. & Novikova, A. A. Study of thermal transformations of aluminum phosphate binder and composites on its basis with various fillers. *Russ. J. Appl. Chem.* **89**, 367–373. https://doi.org/10.1134/S1070427216030046 (2016).
6. Bian, D. & Zhao, Y. Preparation and corrosion mechanism of graphene-reinforced chemically bonded phosphate ceramics. *J. Sol–Gel Sci. Technol.* **80**, 30–37. https://doi.org/10.1007/s10971-016-4061-9 (2016).
7. Chiou, J.-M. & Chung, D. D. L. Improvement of the temperature resistance of aluminium-matrix composites using an acid phosphate binder. *J. Mater. Sci.* **28**, 1435–1446. https://doi.org/10.1007/BF00363335 (1993).
8. Langlet, M., Saltzberg, M. & Shannon, R. D. Aluminium metaphosphate glass-ceramics. *J. Mater. Sci.* **27**, 972–982. https://doi.org/10.1007/BF01197650 (1992).
9. Wang, M. *et al.* Effect of $Al(PO_3)_3$ content on physical, chemical and optical properties of fluorophosphate glasses for 2 μm application. *Mater. Chem. Phys.* **114**, 295–299. https://doi.org/10.1016/j.matchemphys.2008.09.014 (2009).
10. Gan, F., Jiang, Y. & Jiang, F. Formation and structure of $Al(PO_3)_3$-containing fluorophosphate glass. *J. Non. Cryst. Solids* **52**, 263–273. https://doi.org/10.1016/0022-3093(82)90301-5 (1982).
11. Ben Taher, Y., Hajji, R., Oueslati, A. & Gargouri, M. Infra-red, NMR spectroscopy and transport properties of diphosphate $NaAlP_2O_7$. *J. Clust. Sci.* **26**, 1279–1294. https://doi.org/10.1007/s10876-014-0812-3 (2015).
12. Taher, Y. B., Oueslati, A., Khirouni, K. & Gargouri, M. Impedance spectroscopy and conduction mechanism of $LiAlP_2O_7$ material. *Mater. Res. Bull.* **78**, 148–157. https://doi.org/10.1016/j.materresbull.2016.02.033 (2016).
13. Ben Taher, Y., Oueslati, A. & Gargouri, M. ac conductivity and NSPT model conduction of $KAlP_2O_7$ compound. *Ionics (Kiel)* **21**, 1321–1332. https://doi.org/10.1007/s11581-014-1288-8 (2015).
14. Zhu, J. *et al.* Synthesis and red emitting properties of $NaAlP_2O_7:Pr^{3+}$ polycrystal for blue chip-excited WLEDS. *Results Phys.* **12**, 771–775. https://doi.org/10.1016/j.rinp.2018.12.047 (2019).
15. Chen, X., Lv, F., Ma, Y. & Zhang, Y. Preparation and spectroscopic investigation of novel $NaAlP_2O_7:Eu^{2+}$ phosphors for white LEDs. *J. Alloys Compd.* **680**, 20–25. https://doi.org/10.1016/j.jallcom.2016.04.125 (2016).
16. Hao, Y. *et al.* Highly porous aluminophosphates with unique three dimensional open framework structures from mild hydrothermal syntheses. *CrystEngComm* **22**, 3070–3078. https://doi.org/10.1039/d0ce00075b (2020).
17. Komura, K., Aoki, H., Tanaka, K. & Ikeda, T. GAM-3: A zeolite formed from $AlPO_4$-5: Via multistep structural changes. *Chem. Commun.* **56**, 14901–14904. https://doi.org/10.1039/d0cc06086k (2020).
18. Parise, J. B. *et al.* Characterization of Se-Loaded Molecular Sieves A, X, Y, AIPO-5, and Mordenite. *Inorg. Chem.* **27**, 221–228. https://doi.org/10.1021/ic00275a002 (1988).
19. Stoch, P., Stoch, A., Ciecinska, M., Krakowiak, I. & Sitarz, M. Structure of phosphate and iron-phosphate glasses by DFT calculations and FTIR/Raman spectroscopy. *J. Non. Cryst. Solids* **450**, 48–60. https://doi.org/10.1016/j.jnoncrysol.2016.07.027 (2016).
20. Acelas, N. Y., Mejia, S. M., Mondragón, F. & Flórez, E. Density functional theory characterization of phosphate and sulfate adsorption on Fe-(hydr)oxide: Reactivity, pH effect, estimation of Gibbs free energies, and topological analysis of hydrogen bonds. *Comput. Theor. Chem.* **1005**, 16–24. https://doi.org/10.1016/j.comptc.2012.11.002 (2013).
21. Stoch, A., Maurin, J., Kulawik, J. & Stoch, P. Structural properties of multiferroic $0.5BiFeO_3–0.5Pb(Fe_{0.5}Nb_{0.5})O_3$ solid solution. *J. Eur. Ceram. Soc.* **37**, 1467–1476. https://doi.org/10.1016/j.jeurceramsoc.2016.11.029 (2017).
22. Rice, C. *et al.* Raman-scattering measurements and first-principles calculations of strain-induced phonon shifts in monolayer MoS_2. *Phys. Rev. B Condens. Matter Mater. Phys.* **87**, 1–5. https://doi.org/10.1103/PhysRevB.87.081307 (2013).
23. Janzen, B. M., Gillen, R., Galazka, Z., Maultzsch, J. & Wagner, M. R. First and second order Raman spectroscopy of monoclinic β-Ga_2O_3. *Phy. Rev.* **6**, 054601 (2022).
24. Brow, R. K. Review: the structure of simple phosphate glasses. *J. Non-Cryst. Solids* **263**, 1–28. https://doi.org/10.1016/S0022-3093(99)00620-1 (2000).

25. Stachel, D., Svoboda, I. & Fuess, H. Phosphorus pentoxide at 233 K. *Acta Crystallogr. Sect. C Cryst. Struct. Commun.* **51**, 1049–1050. https://doi.org/10.1107/S0108270194012126 (1995).
26. Van der Meer, H. The crystal structure of a monoclinic form of aluminium metaphosphate, $Al(PO_3)_3$. *Acta Crystallogr. B* **32**, 2423–2426. https://doi.org/10.1107/S0567740876007899 (1976).
27. Pauling, L. & Sherman, J. The crystal structure of aluminum metaphosphate, $Al(PO_3)_3$. *Zeitschrift für Krist. - Cryst. Mater.* **96**, 481–487. https://doi.org/10.1524/zkri.1937.96.1.481 (1937).
28. Oudahmane, A., Mbarek, A., El-Ghozzi, M. & Avignant, D. Aluminium cyclohexaphosphate. *Acta Crystallogr. Sect. E Struct. Reports* https://doi.org/10.1107/S1600536810005374 (2010).
29. Vippola, M. *et al.* Structural characterization of aluminum phosphate binder. *J. Am. Ceram. Soc.* **83**, 1834–1836. https://doi.org/10.1111/j.1151-2916.2000.tb01477.x (2000).
30. Bemmer, V. *et al.* Rationalization of the X-ray photoelectron spectroscopy of aluminium phosphates synthesized from different precursors. *RSC Adv.* **10**, 8444–8452. https://doi.org/10.1039/c9ra08738a (2020).
31. Achary, S. N., Jayakumar, O. D., Tyagi, A. K. & Kulshreshthha, S. K. Preparation, phase transition and thermal expansion studies on low-cristobalite type $Al_{1-x}Ga_xPO_4$ (x=0.0, 0.20, 0.50, 0.80 and 1.00). *J. Solid State Chem.* **176**, 37–46. https://doi.org/10.1016/S0022-4596(03)00341-4 (2003).
32. Hummel, F. A. Properties of some substances isostructural with silica. *J. Am. Ceram. Soc.* **32**, 320–326. https://doi.org/10.1111/j.1151-2916.1949.tb18905.x (1949).
33. Muraoka, Y. & Kihara, K. The temperature dependence of the crystal structure of berlinite, a quartz-type form of $AlPO_4$. *Phys. Chem. Miner.* **24**, 243–253. https://doi.org/10.1007/s002690050036 (1997).
34. Graetsch, H. A. High-temperature phase transitions and intermediate incommensurate modulation of the tridymite form of $AlPO_4$. *Zeitschrift fur Krist.* **222**, 226–233. https://doi.org/10.1524/zkri.2007.222.5.226 (2007).
35. Graetsch, H. Two forms of aluminium phosphate tridymite from X-ray powder data. *Acta Crystallogr Sect. C Cryst. Struct. Commun.* **56**, 401–403. https://doi.org/10.1107/S0108270199015164 (2000).
36. Nicola, J. H. & Scott, J. F. Raman study of the α-β cristobalite phase transition in $AlPO_4$. *Phys. Rev. B* **18**, 1972 (1978).
37. Rokita, M., Handke, M. & Mozgawa, W. The $AlPO_4$ polymorphs structure in the light of Raman and IR spectroscopy studies. *J. Mol. Struct.* **555**, 351–356. https://doi.org/10.1016/S0022-2860(00)00620-7 (2000).
38. Westbrook, J. H. Temperature dependence of strength and brittleness of some quartz structures. *J. Am. Ceram. Soc.* **41**, 433–440. https://doi.org/10.1111/j.1151-2916.1958.tb12891.x (1958).
39. Beck, W. R. Crystallographic inversions of the aluminum orthophosphate polymorphs and their relation to those of silica. *J. Am. Ceram. Soc.* **32**, 147–151. https://doi.org/10.1111/j.1151-2916.1949.tb18940.x (1949).
40. Ng, H. N. & Calvo, C. X-ray study of the twinning and phase transformation of phosphocristobalite ($AlPO_4$). *Can. J. Phys.* **55**, 677–683. https://doi.org/10.1139/p77-095 (1977).
41. Saidi, M., Coffy, G. & Sibieude, F. Les systemes binaires $AlPO_4$–M_3PO_4 (M=Li, Na, K). *J. Therm. Anal.* **44**, 15–23. https://doi.org/10.1007/BF02547129 (1995).
42. Zhang, L. & Brow, R. K. A Raman study of iron-phosphate crystalline compounds and glasses. *J. Am. Ceram. Soc.* **94**, 3123–3130. https://doi.org/10.1111/j.1551-2916.2011.04486.x (2011).
43. Okada, S. *et al.* Cathode properties of amorphous and crystalline $FePO_4$. *J. Power Sources* **146**, 570–574. https://doi.org/10.1016/j.jpowsour.2005.03.200 (2005).
44. Rojo, J. M., Mesa, J. L., Lezama, L. & Rojo, T. Magnetic properties of the $Fe(PO_3)_3$ metaphosphate. *J. Solid State Chem.* **145**, 629–633. https://doi.org/10.1006/jssc.1999.8262 (1999).
45. Stoch, P. *et al.* Influence of aluminum on structural properties of iron-polyphosphate glasses. *Ceram. Int.* **46**, 19146–19157. https://doi.org/10.1016/j.ceramint.2020.04.250 (2020).
46. Stoch, P. *et al.* Structural properties of iron-phosphate glasses: spectroscopic studies and ab initio simulations. *Phys. Chem. Chem. Phys.* **16**, 19917–19927. https://doi.org/10.1039/C4CP03113J (2014).
47. Giannozzi, P. *et al.* QUANTUM ESPRESSO: A modular and open-source software project for quantum simulations of materials. *J. Phys. Condens. Matter* https://doi.org/10.1088/0953-8984/21/39/395502 (2009).
48. Alkemper, J., Paulus, H. & Fuei, H. Crystal structure of aluminum sodium pyrophosphate, $NaAlP_2O_7$. *Zeitschrift für Krist. - Cryst. Mater.* **209**, 616–616. https://doi.org/10.1524/zkri.1994.209.7.616 (1994).
49. van Setten, M. J. *et al.* The PSEUDODOJO: Training and grading a 85 element optimized norm-conserving pseudopotential table. *Comput. Phys. Commun.* **226**, 39–54. https://doi.org/10.1016/j.cpc.2018.01.012 (2018).
50. Hamann, D. R. Optimized norm-conserving Vanderbilt pseudopotentials. *Phys Rev. B - Condens. Matter Mater. Phys.* **88**, 1–10. https://doi.org/10.1103/PhysRevB.88.085117 (2013).
51. Virtanen, P. *et al.* SciPy 1.0: Fundamental algorithms for scientific computing in Python. *Nat. Methods* **17**, 261–272. https://doi.org/10.1038/s41592-019-0686-2 (2020).
52. Toby, B. H. & Von Dreele, R. B. GSAS-II: The genesis of a modern open-source all purpose crystallography software package. *J. Appl. Crystallogr.* **46**, 544–549. https://doi.org/10.1107/S0021889813003531 (2013).

Acknowledgements

Author contributions

All authors reviewed the manuscript.B.H. and P.G. conducted research.P.G. performed ab-initio calculations, prepared figures and synthesized the samples.P.S. and P.G. wrote the main manuscript text and analyzed data.

Competing interests

The authors declare no competing interests.

Additional information

Supplementary Information The online version contains supplementary material available at https://doi.org/10.1038/s41598-022-22432-5.

Correspondence and requests for materials should be addressed to P.G.

Reprints and permissions information is available at www.nature.com/reprints.